Model predictive control of a multi-degree-of-freedom wave energy converter with model mismatch and prediction errors

A.J. Hillis[1], J. Yardley[1], A.R. Plummer[1], and A. Brask[2]

[1]University of Bath, Department of Mechanical Engineering, Bath BA27AY, UK (e-mail: a.j.hillis@bath.ac.uk, joshyardley01@gmail.com, a.r.plummer@bath.ac.uk).
[2]Marine Power Systems Ltd, Ethos Building, Kings Road, Swansea, SA1 8AS (e-mail: contact@marinepowersystems.co.uk).

Abstract

The power captured by a wave energy converter (WEC) can be greatly increased through the use of a well-conceived wave-by-wave control strategy. Optimal strategies including Model Predictive Control (MPC) rely on a dynamic model of the WEC and prediction of the wave excitation force several seconds into the future. Both the modelling and prediction processes are subject to errors. This study investigates the impact of these errors on the performance of a WEC under MPC. Idealised simulations are conducted to establish a suitable prediction horizon and establish a performance benchmark against an optimally tuned passively damped system. Power increases of over 200% are seen. The assumptions of perfect prediction and system modelling are progressively removed, culminating in multi-body simulation of a specific multi-DOF submerged point absorber WEC with constrained MPC. Under realistic conditions, the power gain is a more modest 30% at best across the tested sea states, demonstrating that these errors have a significant impact on performance. However, the ability to use constraints to limit motion in high energy seas and the tunability of the control law are valuable attributes for practical deployment. Overall the performance gains demonstrate the benefits of such control strategies for application to multi-DOF WECs.

Keywords–Wave energy converter, model predictive control, real-time estimation, prediction.

I. Introduction

The control system is key to enabling wave energy converters (WECs) to become economically viable by maximising energy capture in variable sea states. Many control strategies have been proposed to achieve a practically implementable optimal or sub-optimal power maximising objective. This study is concerned with the application of model-based optimal control strategies and uses a Model Predictive Control (MPC) formulation.

Many simulation studies on the control of WECs use a simplified buoy constrained to move only in heave, though there are examples using multiple degree-of-freedom (DOF) devices. For example, Abdelkhalik *et al* have applied a pseudo-spectral optimal controller to a 3-DOF floating point absorber which extracts power from heave, surge and pitch motion [1]. Scruggs *et al* [2] developed an optimal causal controller for a tethered device with similarities to the WEC studied here, and an internal model control strategy is applied to a similar device in [3]. Example WEC applications of MPC can be found in [4], [5] and [6] and many variants have been proposed. In each case, the hydrodynamics are approximated by Boundary Element Method (BEM) solutions and embedded within the idealised model around which the MPC is formulated. The controller performance is then established by application to a system with identical dynamics, thus the assumption is that there is no model mismatch. MPC and other optimal strategies also require future knowledge of the wave excitation force. The common assumption is that this knowledge is readily available and many studies will assume perfect prediction over any control horizon. In practice the excitation force must be estimated (again a model-based procedure) and then forecast on-line based upon measurements and historical data. Errors will inevitably be introduced but there are relatively few studies that investigate the more realistic deployable situations. The focus here is not on the improvement of the control, but

rather to test the effects on system performance of removing common assumptions made in other studies.

The sensitivity of an MPC control strategy to model mismatch in the hydrodynamics (mass, damping and stiffness) has been studied in [7] with application to a simulated heaving buoy. The most significant performance degradation was found to be related to mismatch in the hydrodynamic stiffness model. A more generic study of closed-loop sensitivity to hydrodynamic model mismatch was conducted in [8]. The hydrodynamic added mass, radiation damping and hydrostatic stiffness parameters are varied from those fixed in the controller model. Two common control structures are investigated - approximate conjugate control (ACC) and approximate optimal velocity tracking control (AVT). These are applied to a simplified heaving buoy and the sensitivity of power absorption to parameter variations is established. It is found that ACC is sensitive to inertial and stiffness errors while the AVT is less so due to the robust nature of the tracking loop. In both studies perfect knowledge of the future wave excitation over the prediction horizon was assumed, and errors here will inevitably impact on the overall system performance.

Here we study the effects of prediction errors and model mismatch by applying an MPC law to a specific multi-DOF WEC, known as WaveSub, in multiple situations with progressively more realistic assumptions:

1) In section VII the effect of prediction horizon on performance is studied by applying the MPC law to an idealised linear model of the WEC. Both ideal prediction and combined on-line estimation and prediction of the wave excitation force are included.
2) In section VIII, ideal prediction is assumed but the MPC law is applied to a nonlinear WEC model to study the effects of model mismatch.
3) In section IX, constraints on displacement and control force are applied with model mismatch present.
4) In section X, a WEC-Sim ([9]) simulation of the WEC is conducted which includes on-line estimation and prediction of the excitation force. The model includes full kinematic constraints plus further constraints on control forces to avoid slack PTO lines.

The paper is organised as follows. An overview of the WaveSub WEC is provided in section II. Section III provides a description of the linearised equivalent model for use in the controller. The MPC law is described in section IV. Sea states used for assessment are given in section V and a method for wave force estimation and forecasting given in section VI. Simulation results for the idealised and WEC-Sim cases are provided in sections VII to X and conclusions are provided in section XI.

II. Overview of the WaveSub WEC

WaveSub is under development by Marine Power Systems Ltd (MPS). It is a submerged point absorber with a unique multi-tether configuration and variable geometry which can be tuned to the prevailing sea state. A float moves with the waves and reacts against a moored base. The tethers pull on rotational drums which are attached to a PTO. The WEC is designed such that it can be lowered in energetic seas to avoid slam loading and aid survivability. An illustration of a full scale multi-float concept is shown in Figure 1.

This study uses a single section of this device, comprising a single float with four taut tethers connected to individual drums and rotational PTOs. The float geometry and numerical mesh are illustrated in Figure 2 and the block diagram of the complete system is shown in Figure 3. This embodiment of WaveSub uses mechanical gearboxes connected to the PTO drums, which step up the drum speed and step down its torque accordingly. Electrical generators provide resistive or (occasionally) additive torques to extract or inject power according to a control strategy. The tethers are pretensioned to react the float buoyancy and are also connected to mechanical springs which are used to tune the natural frequency of the device to suit the incident sea state. Table I shows the important dimensions of the WEC system.

III. Linearised dynamic system model

The MPC formulation requires a linearised approximation to the WEC and PTO systems. For simplicity we assume the reactor to be fixed as a taut mooring system is used. Therefore, the WEC dynamics can be represented by the state-space system

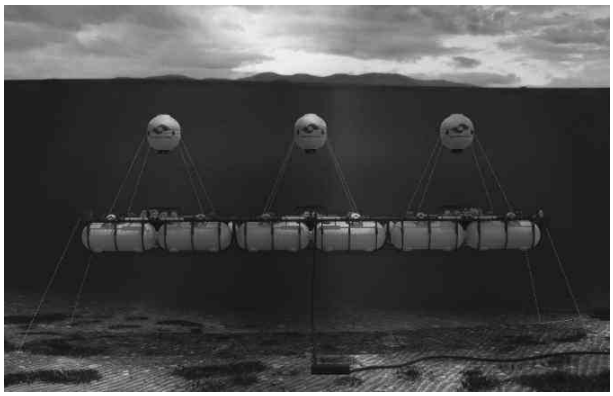

Fig. 1. Illustration of a full scale multi-float WaveSub concept

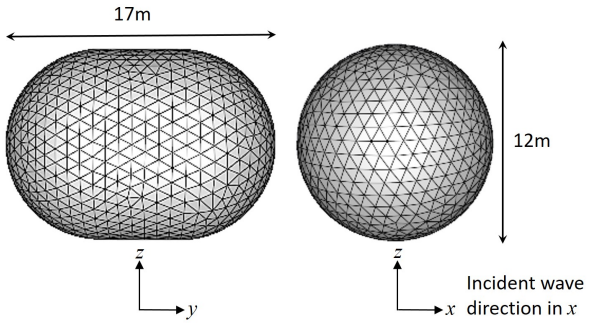

Fig. 2. Float geometry and numerical mesh

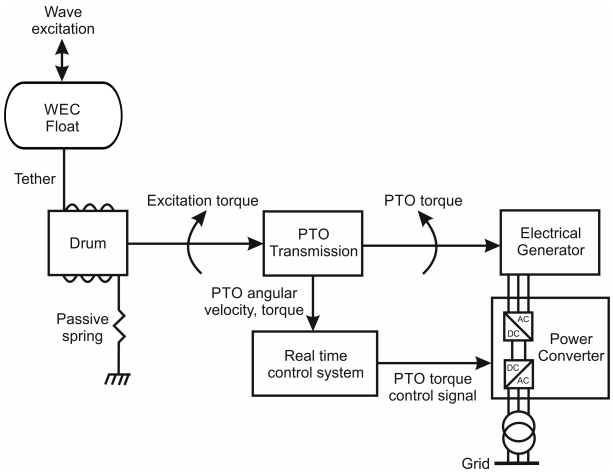

Fig. 3. Block diagram representation of WEC/PTO systems

$$\dot{\mathbf{x}}^{+}(t) = \begin{bmatrix} \dot{\mathbf{x}} \\ \hline \ddot{\mathbf{x}} \\ \hline \dot{\mathbf{p}}_r \end{bmatrix} = \mathbf{A}_c \mathbf{x}^{+}(t) + \mathbf{B}_c(\mathbf{f}_e(t) + \mathbf{u}(t)) \qquad \mathbf{y}(t) = \mathbf{C}_c \mathbf{x}^{+}(t) \tag{1}$$

where $\mathbf{u}$ is the 6DOF control force vector, $\mathbf{f}_e$ is the wave excitation force vector and the position and velocity state vector is given by $[\mathbf{x} \;\; \dot{\mathbf{x}}]^T$. The state vector is augmented with the auxiliary states $\mathbf{p}_r$ relating to a 4^{th} order State-Space approximation $\mathbf{G}_r$ of the radiation impulse response functions

TABLE I
DIMENSIONS OF THE GEOMETRY OF THE FULL SCALE WEC-SIM MODEL

Properties	Value	Unit
Float diameter	12	m
Float cylinder length	4.75	m
Float mass	1184	t
Reactor length	51.55	m
Reactor width	50	m
Reactor height	4.85	m
Water depth	75	m
Submergence (to top of float)	2	m

described by

$$\begin{array}{c} \dot{\mathbf{p}}_r(t) = \mathbf{A}_r \mathbf{p}_r(t) + \mathbf{B}_r \dot{\mathbf{x}}(t) \\ \int_0^t \mathbf{K}_r(t-\tau)\dot{\mathbf{x}}(\tau)d\tau \approx \mathbf{C}_r \mathbf{p}_r(t) + \mathbf{D}_r \dot{\mathbf{x}}(t) \end{array} \tag{2}$$

where the matrices $\{\mathbf{A}_r, \mathbf{B}_r, \mathbf{C}_r, \mathbf{D}_r\}$ describing $\mathbf{G}_r$ are computed using the bemio code supplied with WEC-Sim [9], which uses the radiation impulse response function computed using the NEMOH BEM solver [10]. Including all 36 modes in a general state-space model results in 144 states. For the float geometry studied here (please refer to Figure 2), there are nine significant radiation impulse response functions which need to be approximated (similar to the study in [3]). This results in a reduction to 36 radiation force states and a more tractable model for control system design.

The augmented plant and output matrices are obtained from linearising the WEC system about its nominal resting position. These are given by

$$\mathbf{A}_c = \left[\begin{array}{cc|c} \mathbf{0}^{6\times6} & \mathbf{I}^{6\times6} & \mathbf{0}^{6\times36} \\ -(\mathbf{M}+\mathbf{A}_\infty)^{-1}\mathbf{K}_0 & -(\mathbf{M}+\mathbf{A}_\infty)^{-1}(\mathbf{B}_v+\mathbf{D}_r) & -(\mathbf{M}+\mathbf{A}_\infty)^{-1}\mathbf{C}_r \\ \hline \mathbf{0}^{36\times6} & \mathbf{B}_r & \mathbf{A}_r \end{array}\right] \tag{3}$$

$$\mathbf{B}_c = \left[\begin{array}{c} \mathbf{0}^{6\times6} \\ (\mathbf{M}+\mathbf{A}_\infty)^{-1} \\ \hline \mathbf{0}^{36\times6} \end{array}\right] \tag{4}$$

$$\mathbf{C}_c = \left[\begin{array}{c|c} \mathbf{I}^{12\times12} & \mathbf{0}^{12\times36} \end{array}\right] \tag{5}$$

where $\mathbf{A}_\infty$ is obtained from the BEM solution, $\mathbf{B}_v$ is a linear viscous damping matrix empirically tuned to experimental data [11], and $\mathbf{K}_0$ is the linearised stiffness matrix (see [2]) comprising pretension and PTO spring stiffness terms with the form:

$$\left[\begin{array}{cccccc} k_{xx} & 0 & 0 & 0 & k_{x,\theta_y} & 0 \\ 0 & k_{yy} & 0 & k_{y,\theta_x} & 0 & 0 \\ 0 & 0 & k_{zz} & 0 & 0 & 0 \\ 0 & k_{y,\theta_x} & 0 & k_{\theta_x,\theta_x} & 0 & 0 \\ k_{x,\theta_y} & 0 & 0 & 0 & k_{\theta_y,\theta_y} & 0 \\ 0 & 0 & 0 & 0 & 0 & k_{\theta_z,\theta_z} \end{array}\right] \tag{6}$$

The state-space model is then discretized using a first-order hold approximation, such that

$$\begin{array}{c} \mathbf{x}_{k+1}^+ = \mathbf{A}\mathbf{x}_k^+ + \mathbf{B}(\mathbf{f}_{ek} + \mathbf{u}_k) \\ \mathbf{y}_k = \mathbf{C}\mathbf{x}_k^+ \end{array} \tag{7}$$

IV. MODEL PREDICTIVE CONTROL

The predicted state trajectory over the prediction horizon N is generated from the discrete time state-space model (7) according to

$$\mathbf{X}_k^+ = \boldsymbol{\mathcal{M}}\boldsymbol{x}_k^+ + \boldsymbol{\mathcal{C}}(\hat{\mathbf{F}}_{e|k} + \mathbf{U}_k) \tag{8}$$

where $\mathbf{U}_k$ and $\hat{\mathbf{F}}_{e|k}$ are the stacked future control force and estimated excitation force matrices given by

$$\mathbf{U}_k = \begin{bmatrix} \mathbf{u}_k \\ \mathbf{u}_{k+1} \\ \vdots \\ \mathbf{u}_{k+N-1} \end{bmatrix} \quad \hat{\mathbf{F}}_{e|k} = \begin{bmatrix} \hat{\mathbf{f}}_{e|k} \\ \hat{\mathbf{f}}_{e|k+1} \\ \vdots \\ \hat{\mathbf{f}}_{e|k+N-1} \end{bmatrix} \tag{9}$$

$$\boldsymbol{\mathcal{M}} = \begin{bmatrix} \mathbf{A} \\ \mathbf{A}^2 \\ \vdots \\ \mathbf{A}^N \end{bmatrix} \qquad \boldsymbol{\mathcal{C}} = \begin{bmatrix} \mathbf{B} & \mathbf{0} & \cdots & \mathbf{0} \\ \mathbf{AB} & \mathbf{B} & \cdots & \mathbf{0} \\ \vdots & \vdots & \ddots & \\ \mathbf{A}^{N-1}\mathbf{B} & \mathbf{A}^{N-2}\mathbf{B} & \cdots & \mathbf{B} \end{bmatrix} \tag{10}$$

The control objective is to maximise the average absorbed power $\bar{w}$ over the prediction horizon through appropriate manipulation of the control force $\mathbf{u}$. This objective can be expressed as the discrete integral [12]

$$\bar{w} = \frac{1}{N} \sum_{i=k}^{k+N} \mathbf{x}_i^+ \mathbf{s} \mathbf{u}_i = \mathbf{X}^{+^T} \mathbf{S} \mathbf{U} \tag{11}$$

where

$$\mathbf{s} = \begin{bmatrix} \mathbf{0}^{6\times6} & \mathbf{I}^{6\times6} & \mathbf{0}^{6\times36} \end{bmatrix}^T \tag{12}$$

and $\mathbf{S} \in \Re^{48N\times6N}$ is the N-block-diagonal matrix of $\mathbf{s}$:

$$\mathbf{S} = \begin{bmatrix} \mathbf{s} & \mathbf{0} & \mathbf{0} \\ \mathbf{0} & \ddots & \mathbf{0} \\ \mathbf{0} & \mathbf{0} & \mathbf{s} \end{bmatrix} \tag{13}$$

Substituting the state prediction (8) into the objective function (11) gives the quadratic cost function

$$J(\mathbf{U}_k) = \mathbf{U}_k^T \mathbf{H} \mathbf{U}_k + \mathbf{F}^T \mathbf{U}_k \tag{14}$$

where $\mathbf{H} = \boldsymbol{\mathcal{C}}^T \mathbf{S}$, $\mathbf{F}^T = \mathbf{X}_k^{+T} \boldsymbol{\mathcal{M}}^T \mathbf{S} + \hat{\mathbf{F}}_{e|k}^T \boldsymbol{\mathcal{C}}^T \mathbf{S}$. Since $\mathbf{H}$ is time-invariant it is computed offline, while $\mathbf{F}^T$ is updated each time step according to the most recent estimates of the state prediction $\mathbf{X}_k^+$ and forecast excitation force $\hat{\mathbf{F}}_{e|k}$. To improve the tractability of the optimisation, the cost function is convexified with the addition of small diagonal terms to $\mathbf{H}$ equal to the absolute value of its smallest eigenvalue ([13]), such that $\hat{\mathbf{H}} = \mathbf{H} + |\lambda_{min}|(\mathbf{H})$. It should be noted that other terms can readily be included within the cost function. Common examples include rate penalties on the control signal to restrict actuation bandwidth, and a penalty on power flow from the grid into the actuator (and ultimately a passivity constraint to eliminate this entirely). These are not included here as the focus of the study is to explore the effects of model and prediction errors on performance. Including additional variables could dilute these effects.

With the addition of state constraints designed to limit surge and heave position amplitudes, and limits on the control force, the optimisation problem is defined as

$$\begin{aligned} &\underset{\mathbf{U}_k}{\text{maximise}} \quad \mathbf{U}_k^T \hat{\mathbf{H}} \mathbf{U}_k + \mathbf{F}^T \mathbf{U}_k \\ &\text{subject to} \quad \begin{bmatrix} \mathbf{I} \\ \mathbf{-I} \\ \boldsymbol{\mathcal{C}}_i \\ -\boldsymbol{\mathcal{C}}_i \end{bmatrix} \mathbf{u}\,[k] \leq \begin{bmatrix} \bar{\mathbf{u}} \\ -\bar{\mathbf{u}} \\ \bar{\mathbf{x}} \\ -\underline{\mathbf{x}} \end{bmatrix} + \begin{bmatrix} \mathbf{0} \\ \mathbf{0} \\ -\mathbf{A}^i \\ \mathbf{A}^i \end{bmatrix} \mathbf{x}_k^+ \;, \quad i = 1:N \end{aligned} \tag{15}$$

where $\bar{\mathbf{x}}$ and $\underline{\mathbf{x}}$ are the upper and lower bounds of the state variables, respectively, and $\bar{\mathbf{u}}$ is the upper limit on control force. There is a necessary additional constraint on control force to avoid slack

PTO tethers, but including this in the optimisation can result in constraint conflict and subsequent intractability of the solution. Therefore this constraint is imposed as a dynamic saturation on the control force post optimisation, exactly as it is for the passive system.

Performing this optimisation and applying only the output for the next time step to the WEC results in a 6DOF control force in Cartesian space. This control force vector is applied to idealised models in sections VII to IX. For WEC-Sim simulations conducted in section X, the control force is distributed to the four PTO tethers according to

$$\mathbf{u}_{PTO} = \mathbf{J}_0^T \mathbf{u} \tag{16}$$

where $\mathbf{J}_0^T$ is the transpose of the kinematic Jacobian matrix. The inverse kinematic matrix relates Cartesian and PTO tether spaces, and is given by [2]

$$\mathbf{J}_0^{-1} = \begin{bmatrix} \mathbf{e}_{s1}^T & (\mathbf{F}_1 \times \mathbf{e}_{s1})^T \\ \vdots & \vdots \\ \mathbf{e}_{s4}^T & (\mathbf{F}_4 \times \mathbf{e}_{s4})^T \end{bmatrix} \tag{17}$$

With reference to Figure 4, $\mathbf{F}_i$ is the the float connection point coordinate vector relative to the float centre of gravity and $\mathbf{e}_{si}$ is the unit vector along the direction of the i^{th} PTO tether in the nominal WEC position.

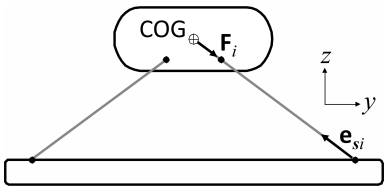

Fig. 4. Illustration of WEC kinematics

It should be noted that, for the head-on wave loading cases studied here, and due to the symmetry of the WEC float, the PTOs act in pairs. It would therefore be possible to reduce the control problem to two inputs and reduce the computational burden. However, the general case for off-axis loading requires control in all DOFs and the PTOs will have to behave independently. Future work will study these aspects of the problem, so we maintain generality here.

V. Sea states

Three irregular sea states were selected for this study, covering the full range of expected energy periods and significant wave heights. All spectra are Pierson-Moskowitz (PM) type and identical time-domain wave elevation sequences are applied across all simulations to enable fair comparison between the performance of the passive and actively controlled systems.

The PM wave height spectrum for a frequency ω [rad/s] is defined by

$$S(\omega) = \frac{\alpha g^2}{\omega^5} \exp\left[-1.25\left(\frac{\omega_\mathrm{p}}{\omega}\right)^4\right] \tag{18}$$

where g is gravitational acceleration and ω_p is the peak frequency. This spectrum has a peak period $T_p = 2\pi/\omega_p$ and the energy period is defined as $T_e = 0.82T_p$. The parameter α is used to adjust the spectrum for a defined significant wave height H_s according to the relationship

$$\alpha = \frac{H_s^2}{16 \int_0^\infty S(\omega) \mathrm{d}\omega} \tag{19}$$

The three spectra and time-domain plots are shown in Figure 5.

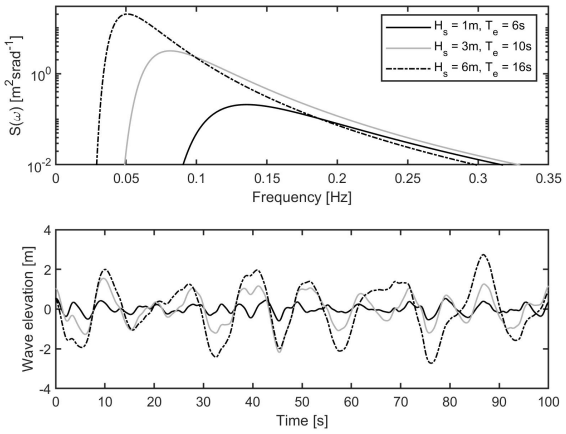

Fig. 5. Irregular sea states used for simulation studies

VI. Wave excitation force

A. Estimation

The wave excitation or disturbance force is not measurable, but is a necessary input to the optimisation problem in order to generate the appropriate control force. In order to estimate the disturbance force it is required to know the dynamics of the float body and all other forces acting upon it, as well as estimates or measurements of the float motion. Float motion and all forces other than the excitation force are readily measured or estimated in practice. It is then possible to implement a dynamic observer to estimate the wave excitation force. Here we use a Kalman Filter approach as described in [14], to estimate the excitation force. As we are able to measure the tether forces directly using load cells, we can directly measure the combination of control force and passive spring force.

The state vector $\mathbf{x}^+$ is further augmented with the estimated unknown force $\mathbf{f}_e$. Maintaining the notation $\mathbf{x}^+$ for the further augmented state vector for convenience, the discretized system dynamics are now described by

$$\begin{aligned} \mathbf{x}^+_{k+1} &= \begin{bmatrix} \mathbf{x}^+ \\ \mathbf{f}_e \end{bmatrix}_{k+1} = \mathbf{A}^+\mathbf{x}^+_k + \mathbf{B}^+ \left(\mathbf{f}_e - \mathbf{T}\right)_k + \boldsymbol{\epsilon}_k \\ \mathbf{y} &= \mathbf{C}^+\mathbf{x}^+_k + \boldsymbol{\mu}_k \end{aligned} \tag{20}$$

where $\boldsymbol{\epsilon}$ describes the random walk process for excitation force estimation and unmodelled dynamics, and $\boldsymbol{\mu}$ describes measurement noise. $\mathbf{T}$ is the Cartesian vector of PTO forces, derived from direct measurement of the combined control and spring forces as PTO tether tensions $\mathbf{T}_{PTO}$, according to

$$\mathbf{T} = \mathbf{J}_0^{-T}\mathbf{T}_{PTO} \tag{21}$$

The system matrices are defined as follows:

$$\mathbf{A}^+ = \begin{bmatrix} \mathbf{A} & \mathbf{B} \\ \mathbf{0} & \mathbf{I} \end{bmatrix} \quad \mathbf{B}^+ = \begin{bmatrix} \mathbf{B} \\ \mathbf{0} \end{bmatrix} \quad \mathbf{C}^+ = \begin{bmatrix} \mathbf{C} & \mathbf{0} \end{bmatrix} \tag{22}$$

The prediction step estimates the next state $\hat{\mathbf{x}}^+_{k|k-1}$ and covariance $\mathbf{P}^+_{k|k-1}$ matrices as:

$$\begin{aligned} \hat{\mathbf{x}}^+_{k|k-1} &= \mathbf{A}^+_{k-1}\hat{\mathbf{x}}^+_{k-1|k-1} + \mathbf{B}^+\mathbf{T}_{k-1|k-1} \\ \mathbf{P}^+_{k|k-1} &= \mathbf{J}^+_{k-1}\mathbf{P}^+_{k-1|k-1}\mathbf{J}^{+T}_{k-1} + \mathbf{Q}^+_{k-1} \end{aligned} \tag{23}$$

where $\mathbf{Q}^+$ is the process noise covariance matrix, which is assumed to represent a zero mean Gaussian process and is empirically tuned. The update step is defined by:

$$
\begin{aligned}
\mathbf{S}_k^+ &= \mathbf{C}^+\mathbf{P}_k^+\mathbf{C}^{+T} + \mathbf{R}_k^+ \\
\mathbf{K}_k^+ &= \mathbf{P}_k^+\mathbf{C}^{+T}\mathbf{S}_k^{+^{-1}} \\
\hat{\mathbf{x}}_{k|k}^+ &= \hat{\mathbf{x}}_{k|k-1}^+ + \mathbf{K}_k^+\left(\begin{bmatrix}\mathbf{y}_k & \hat{\mathbf{f}}_e\end{bmatrix}^T - \mathbf{C}^+\hat{\mathbf{x}}_{k|k-1}^+\right) \\
\mathbf{P}_{k|k}^+ &= (I - \mathbf{K}_k^+\mathbf{C}^+)\mathbf{P}_{k|k-1}^+
\end{aligned}
\tag{24}
$$

where $\mathbf{S}^+$ is the innovation residual, $\mathbf{R}^+$ is the observation covariance associated with the observed value $\mathbf{y}$, and $\mathbf{K}^+$ is the Kalman gain. $\mathbf{J}^+$ is the Jacobian of $\mathbf{A}^+$. For a time invariant state transition matrix (as assumed here) this is equal to $\mathbf{A}^+$.

Figure 6 shows good estimation of the excitation force for surge and heave directions. The result is presented only for one sea state for brevity. In all simulations, the true excitation force is calculated in the standard way using a prescribed wave elevation and hydrodynamic excitation coefficients estimated using the NEMOH BEM solver.

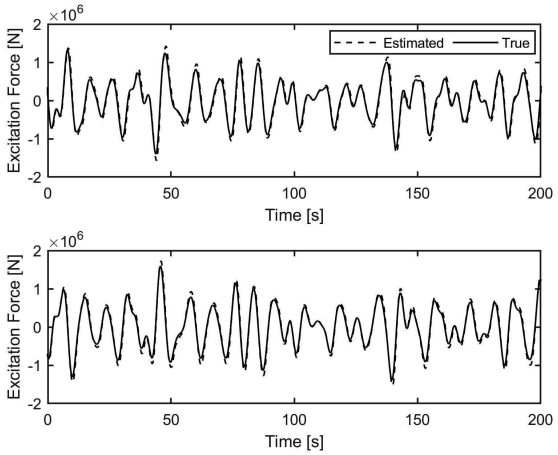

Fig. 6. Estimation of wave excitation force in surge (TOP) and heave (BOTTOM) directions in irregular waves (Pierson-Moskowitz with $H_s = 3$m, $T_e = 10$s)

B. Prediction

The estimated wave excitation force must also be forecast over a prediction horizon for the MPC optimisation. In practice the choice of horizon must balance the improvement in power absorption from the optimisation against the quality of the estimated wave force, which degrades as the forecast horizon increases. Inevitably there will be a point where the estimation is not accurate enough to yield power increases. A further limitation is the computational load, which increases as the prediction horizon increases but must be completed between computational steps.

A number of methods for prediction are studied in [15]. Based on this study an auto-regressive (AR) modelling technique is adopted here. It should be noted that the prediction method is not the focus of this paper. It is sufficient to find a method which gives prediction estimates with a quality comparable with the findings in [15] and which would be implementable in practice.

The N-step ahead prediction of the excitation force at instant k is given by

$$
\hat{\mathbf{f}}_e\left[k+N|k\right] = \sum_{i=1}^{n} \hat{a}_i \hat{\mathbf{f}}_e\left[k+N-i|k\right] \tag{25}
$$

where $\hat{a}_i$ are the AR coefficients resulting from an estimation procedure. Here we use the Burg method to estimate the AR parameters. The training data used for this estimation is excitation force data generated for sea states with the same spectra, but different random seeds (and hence different time-domain values in the sequences). An AR filter with order 200 was found to give acceptable

results with a sampling time of 0.1s. This is sufficient to capture a full wave period in the lowest frequency sea state, and several periods in the highest frequency sea state.

Figure 7 shows the goodness-of-fit for the three sea states of Figure 5 and with a range of prediction horizons. We observe reasonable estimation with the quality reducing as the prediction horizon and energy period of the sea states increase.

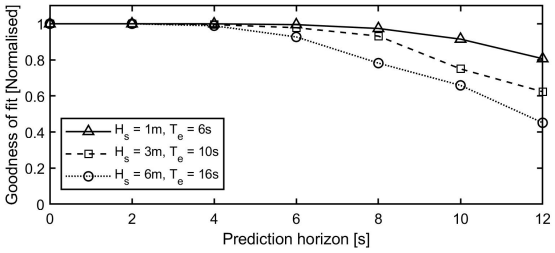

Fig. 7. Goodness of fit of wave excitation force predictions for a range of horizons and sea states

The time-domain plot of the "actual" excitation force (from WEC-Sim simulations) versus the 8s ahead predictions for the surge direction for the three sea states are shown in Figure 8 by way of example.

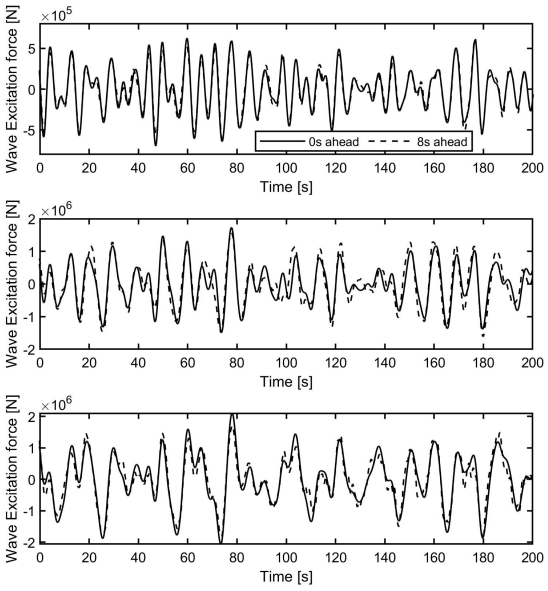

Fig. 8. Actual vs 8s ahead predictions of wave excitation forces. TOP: $H_s = 1$m, $T_e = 6$s, MIDDLE: $H_s = 3$m, $T_e = 10$s, BOTTOM: $H_s = 6$m, $T_e = 16$s

VII. Simulation results: effects of excitation force prediction errors

A simulation study was conducted whereby the system under control is an exact match for the state-space model embedded within the MPC optimisation. Many optimal control studies for WECs are limited to this ideal case, for example [4], [5]. Constraints are not applied at this stage to isolate the effects of prediction errors and to establish the maximum theoretical power gains. The PTO tethers are not modelled, and control forces are assumed to be directly applied to the float COG in the Cartesian frame. As a benchmark for performance comparison, a passively controlled system (i.e. the PTO forces are proportional to the float velocities by the damping constant λ) was tuned for each sea state. Figure 9 shows the tuning results for selecting the optimum damping coefficients.

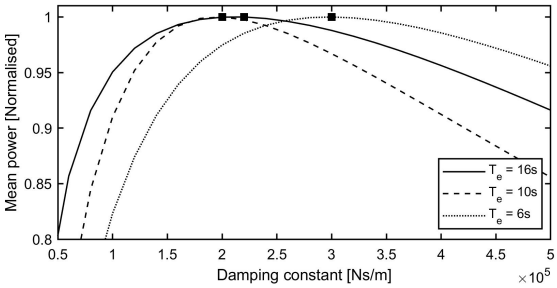

Fig. 9. Tuning results showing optimal passive damping coefficients in tested sea states

The block diagram illustrating these passively damped simulations is shown in Figure 10. In all simulations throughout this paper, a base sample rate of 50Hz was applied and, where appropriate, prediction and MPC blocks use a 10Hz sampling rate. The higher sampling rate is required for stability and accuracy in latter multi-body simulations, while the lower sampling rate is used to reduce computational times without compromising accuracy.

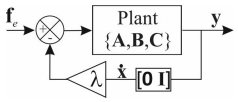

Fig. 10. Block diagram of baseline idealised state-space WEC model simulation with passive damping

The ideal system was then placed under MPC with both ideal prediction and real-time prediction scenarios with a range of prediction horizons. Additionally, the state-space WEC plant model may be time-varying for use in the following section. The block diagram representing these scenarios is illustrated in Figure 11.

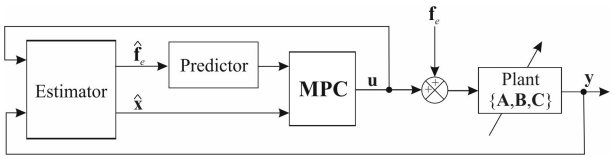

Fig. 11. Block diagram of MPC simulations using fixed or time-varying state-space WEC model

Absorbed power is calculated as the sum of the product of force/torque and velocity/angular velocity in the surge, heave and pitch DOFs. Results are presented for ideal prediction and real-time prediction implemented as described in section VI-B. Figure 12 shows the results for mean power absorbed for each case.

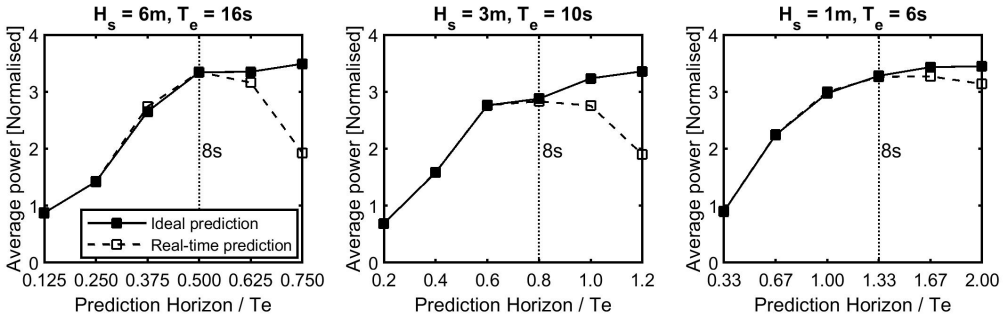

Fig. 12. Mean power absorbed for different horizons with and without real-time prediction of excitation force for idealised system

The power is normalised against the optimal power captured with the passively damped system for each sea state. The time axis is normalised against the energy period of the relevant sea state. It is seen that a horizon of at least 3s is required to increase absorbed power compared to the optimal passive case in all three sea states. We also see the expected reduction in power as the horizon increases for the cases where online prediction is used. Again, as expected this effect is most pronounced for the sea state with the highest energy period as this case has the least accurate forecasting. Based on this and the fact that beyond an 8s horizon the benefits drop off, a pragmatic horizon to use would seem to be 8s, which is in line with other studies. The mean power gains for MPC with real-time prediction compared to the tuned passive system are rather dramatic, being up to a factor of > 3.

VIII. Simulation results: effects of model mismatch

Many previous studies assume that the system under control is precisely represented by the model embedded in the MPC control law. In reality this will never be the case as the system is nonlinear and subject to variation over time due to various forms of degradation. The WaveSub WEC is inherently nonlinear as the system stiffness matrix is dependent on the relative position of the float and reactor. Quadratic viscous drag is also a source of nonlinearity, though this is often considered negligible in comparison to other forces acting on the WEC. This is demonstrated experimentally in [16], for example. In this section, the MPC law remains as before - using the idealised model linearised about its nominal resting position (see equation 7), but the system under control is time-varying as the stiffness matrix is recomputed at each time step. As in the previous section, constraints are not applied at this stage to isolate the effects of model mismatch.

Figure 13 shows the variation of the terms in the stiffness matrix as the float heave (x) and surge (z) positions are varied. Significant variation can be seen across the expected range of travel of the float, so it is important to investigate the effect this will have on the performance of the control law.

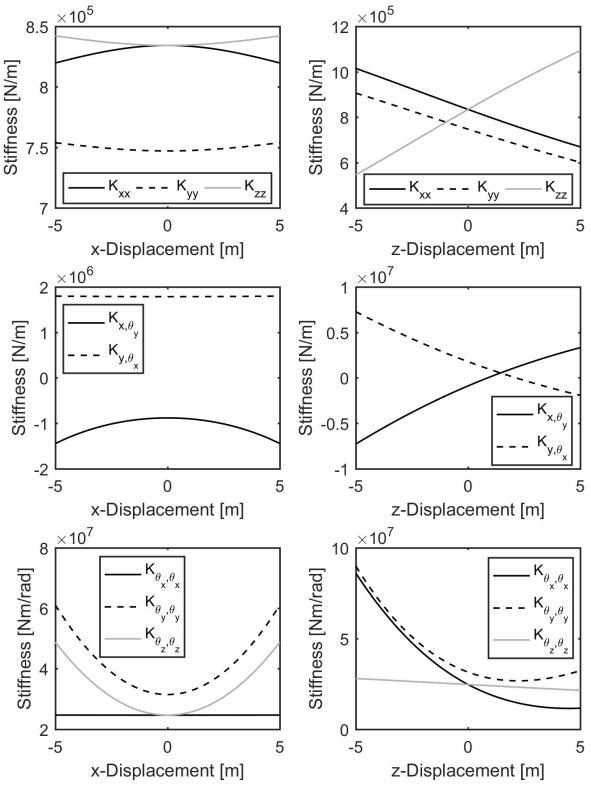

Fig. 13. Variation of terms in WEC stiffness matrix as float position changes

This time-varying system was placed under MPC with ideal prediction and the average captured power compared to that achieved with no model mismatch for a range of prediction horizons (the latter data set is identical to the ideal prediction dataset in Figure 12). Figure 14 shows the results for mean power absorbed for each case. As before, the power is normalised against the optimal power captured with the passively damped system for each sea state. Large differences in captured power are seen when model mismatch is present. For the 16s period seastate there is a substantial reduction in captured power, while the 6s and 10s period sea states show substantial increases in captured power for prediction horizons longer than 4s. To understand the reasons for these differences, it is beneficial to examine the motions and control forces.

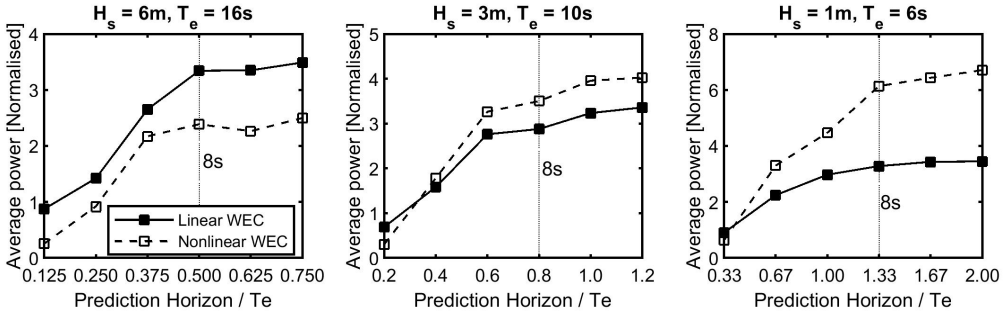

Fig. 14. Mean power absorbed for different horizons with linear and nonlinear WECs

The following results all use an 8s prediction horizon, based on the findings of section VII. Figures 15 to 17 show the surge, heave and pitch displacements for the three sea states.

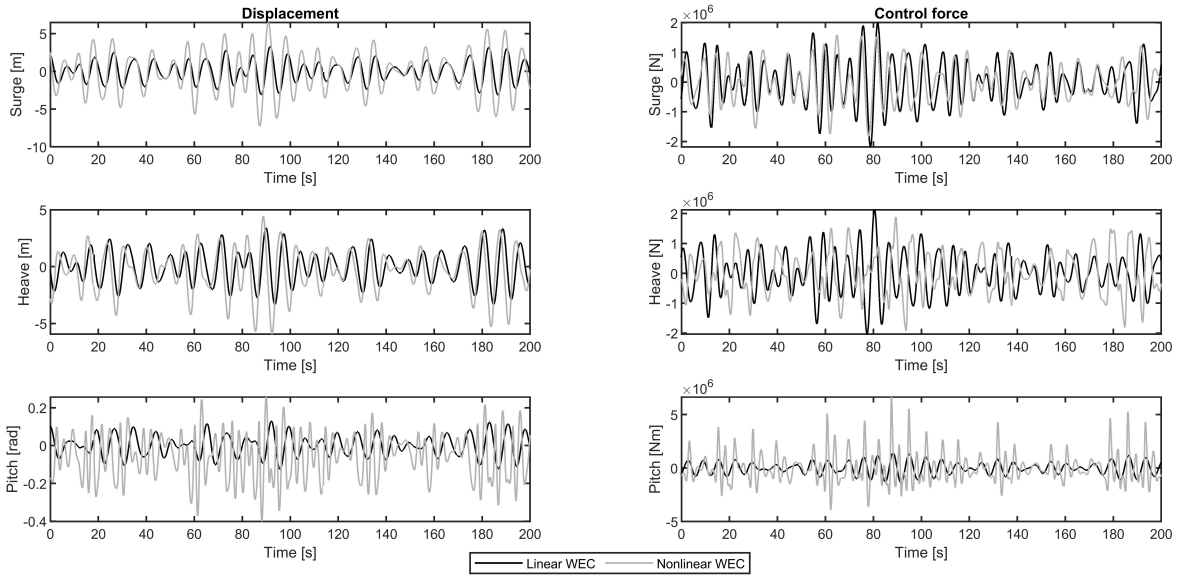

Fig. 15. Surge, heave and pitch float displacements and control forces for linear and nonlinear WECs under MPC for irregular sea state ($H_s = 1$m, $T_e = 6$s)

For sea states with energy periods of 6s and 10s we see increased motion amplitudes with a nonlinear WEC model (this is particularly apparent for the 6s period sea state in Figure 15). The accompanying nonlinear WEC control forces also show small increases, resulting in increased power capture. Figure 17 shows reduced motion with a nonlinear WEC with similar levels of force, resulting in reduced power capture with a nonlinear WEC. A further observation is that the motions are unrealistically large in the more energetic sea states, resulting in substantial changes in the WEC

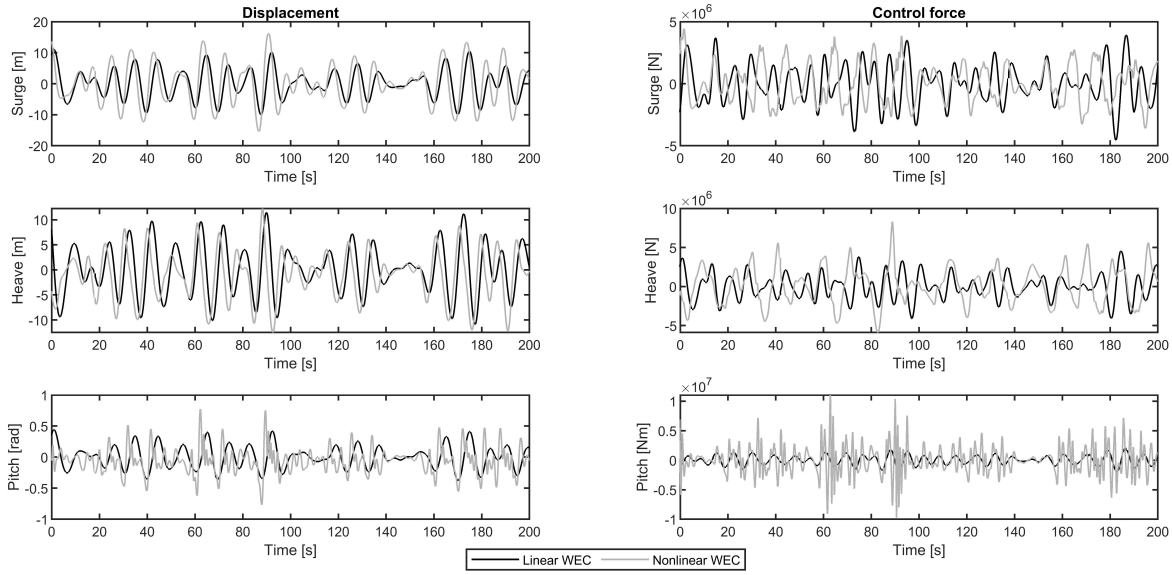

Fig. 16. Surge, heave and pitch float displacements and control forces for linear and nonlinear WECs under MPC for irregular sea state ($H_s = 3$m, $T_e = 10$s)

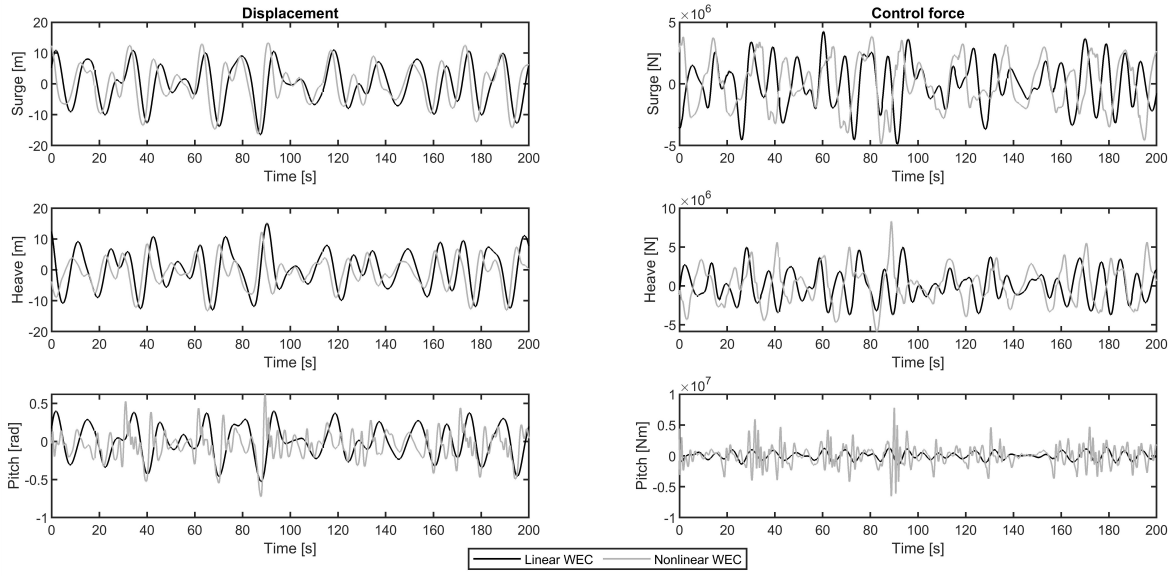

Fig. 17. Surge, heave and pitch float displacements and control forces for linear and nonlinear WECs under MPC for irregular sea state ($H_s = 6$m, $T_e = 16$s)

stiffness matrix (see Figure 13) which the WEC model embedded within the MPC law does not capture. This is the reason for the differences in the results seen here, which suggest that model mismatch can be a significant factor in the performance of MPC with a WEC. However, we cannot come to this conclusion for this application as the motions are not realistic. Of course, one of the most significant benefits of MPC over some other control strategies is the ability to incorporate constraints. In the following section, the more realistic constrained solution is studied.

IX. Simulation results: constrained MPC with model mismatch

A real WEC will have multiple constraints in operation. Here we apply constraints on the surge and heave displacement amplitudes to maintain motion within limits imposed by other structural components of the WEC, and also a control force limit to represent the torque limit of the PTO

generators. Here the surge and heave displacement limits are set at $\pm$3m and $\pm$5m respectively, while the control force limit is set at $\pm$5MN. The torque limit is chosen to enable optimal control across all tested sea states, in reality it may be set lower based on a cost study and it would be accepted that the generator is saturated in higher energy sea states. Figures 18 to 20 show the displacements and forces for the three tested sea states.

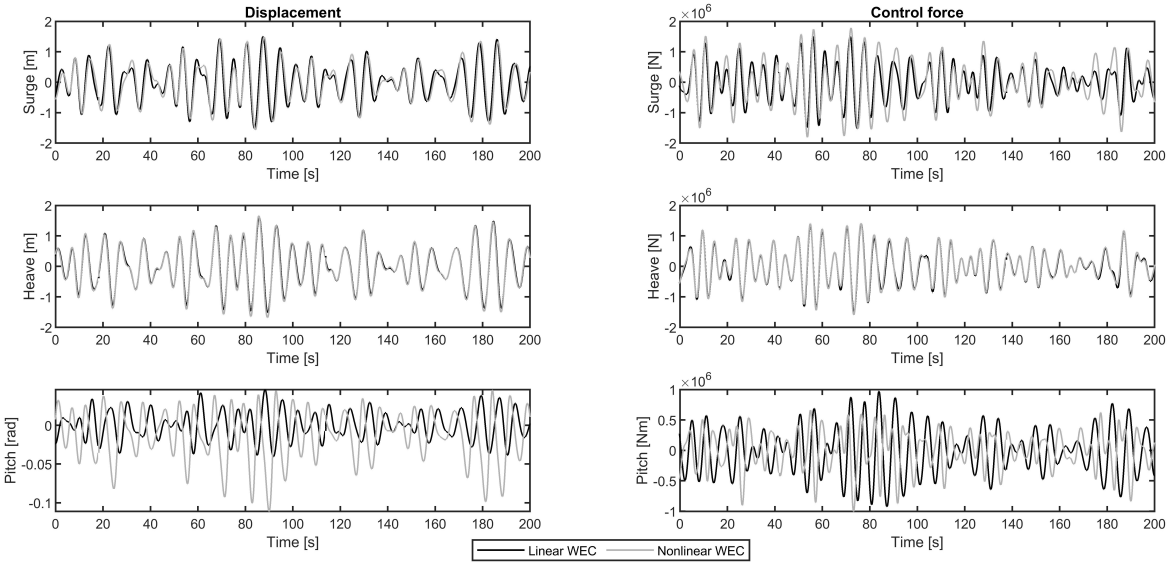

Fig. 18. Surge, heave and pitch float displacements and control forces for linear and nonlinear WECs under MPC for irregular sea state ($H_s = 1$m, $T_e = 6$s)

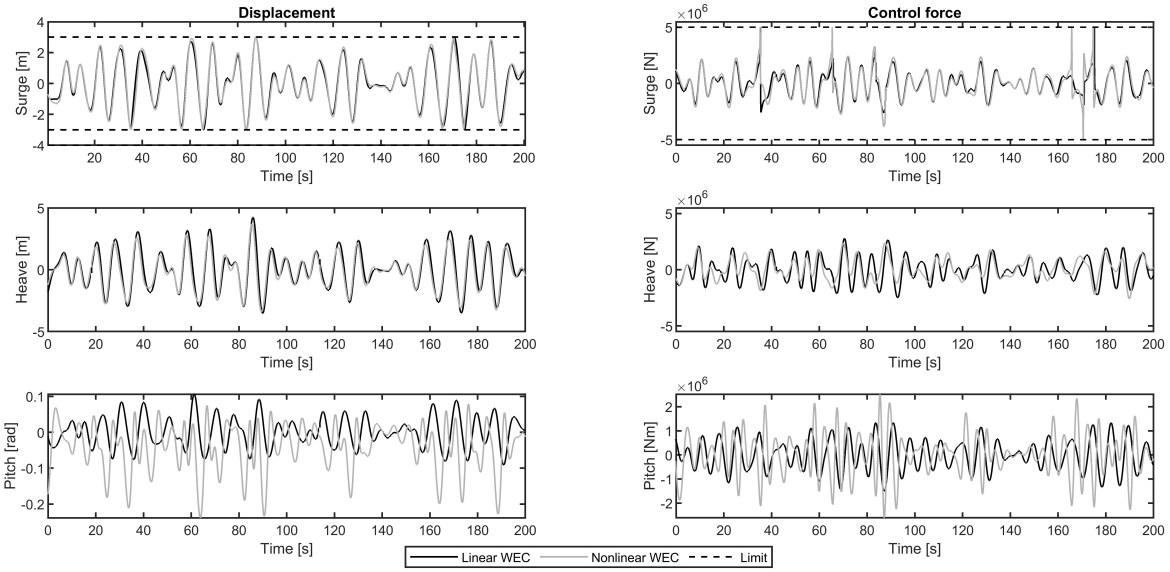

Fig. 19. Surge, heave and pitch float displacements and control forces for linear and nonlinear WECs under MPC for irregular sea state ($H_s = 3$m, $T_e = 10$s)

As before, these results are achieved using an 8s prediction horizon as this generated the maximum average power in the tested sea states. They show the comparison of results using a linear WEC and a nonlinear WEC. The purpose of these results is to investigate in isolation the effects of model mismatch under constrained control. It is seen that the differences are far less pronounced than for the unconstrained control cases (see Figures 15 to 17). This is to be expected since the constraining of the displacements reduces the stiffness changes in the nonlinear WEC.

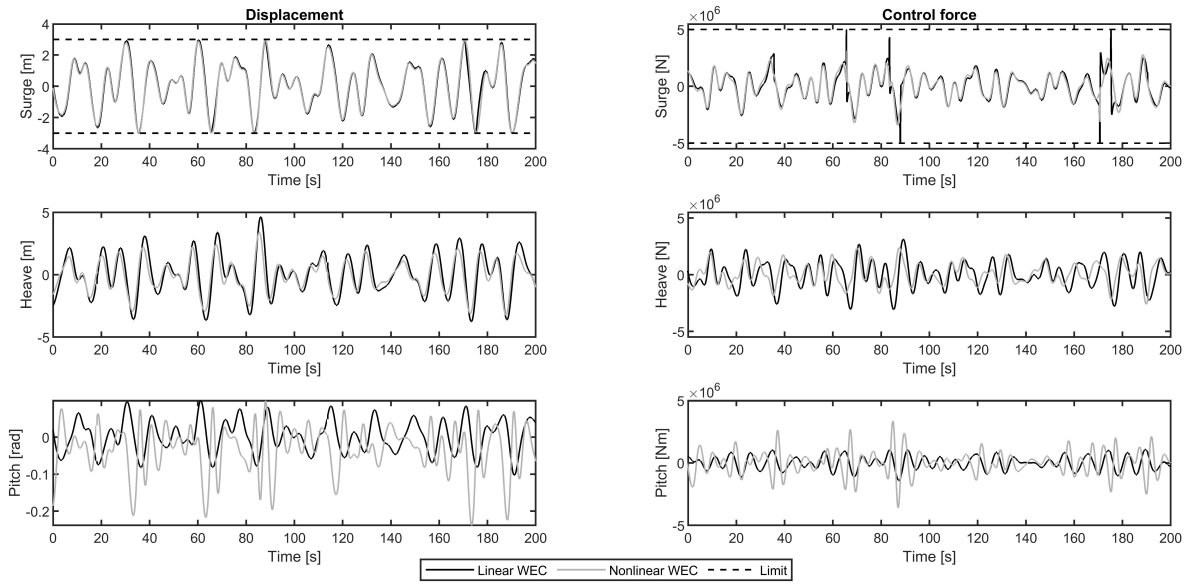

Fig. 20. Surge, heave and pitch float displacements and control forces for linear and nonlinear WECs under MPC for irregular sea state ($H_s = 6$m, $T_e = 16$s)

The instantaneous captured power for constrained MPC with linear and nonlinear WECs is shown in Figure 21.

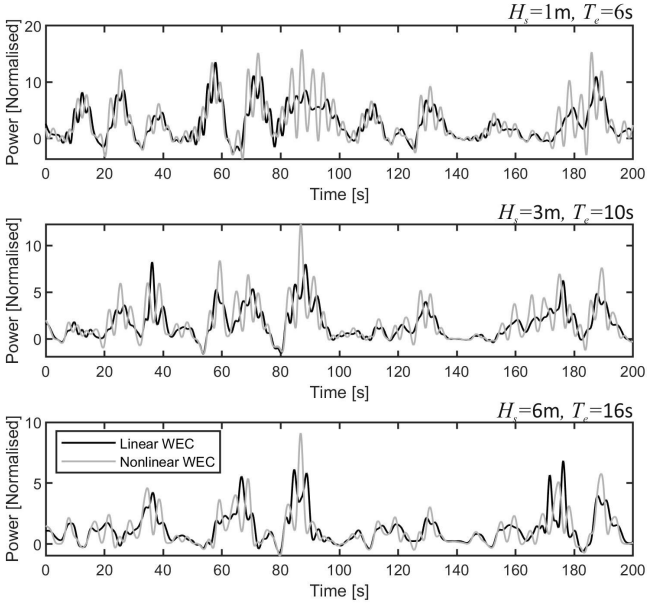

Fig. 21. Instantaneous captured power for constrained MPC with linear and nonlinear WECS in irregular sea states

Table II shows the comparison of mean captured power compared to the optimally tuned passive system. For comparative purposes, the mean powers achieved with unconstrained MPC with an 8s prediction horizon are also included.

Despite the constraints, we see very large increases still in mean power capture compared to the optimal passive system. As for the unconstrained MPC there is a slight increase in captured power for the nonlinear WEC compared with the linear WEC. The action of the constraints means that

TABLE II
MEAN POWER INCREASES COMPARED TO TUNED PASSIVE SYSTEM

Sea State		Mean power ratio (MPC/passive)			
		Unconstrained		Constrained	
T_e[s]	H_s[m]	Linear WEC	Nonlinear WEC	Linear WEC	Nonlinear WEC
6	1	3.28	6.14	2.47	2.62
10	3	2.89	3.50	1.51	1.66
16	6	3.34	2.39	1.24	1.15

the captured power is reduced compared to the unconstrained results in the previous section. These results suggest that substantial gains can be achieved using a constrained MPC strategy compared to an optimally tuned passive strategy even when there is realistic model mismatch between the MPC embedded model and the controlled system. However, this WEC model is still somewhat idealised and does not capture some of the additional complications and constraints that would exist with the deployed physical system. The next section addresses this.

X. SIMULATION RESULTS: DEPLOYABLE MPC WITH WEC-SIM MULTI-BODY WEC MODEL

The MPC constrained optimisation together with estimation and real-time prediction of the excitation force is now applied to a nonlinear WEC-Sim model of the multi-DOF WEC. Here only quantities that are measurable on a physical system are used in the control, estimation and forecasting procedures. Additionally the control action is through the PTO lines and not in Cartesian space and quadratic viscous damping is included. These simulations, therefore, represent a more realistic scenario as the controller is deployable in a real system and there is model mismatch between the state-space idealisation embedded within the optimisation and the system under control. Results in this section are compared to the optimally tuned passive system, where both the PTO line stiffness and damping ratio are tuned to each sea state. This benchmark has been used in previous studies, for example [17]. A 10s prediction horizon was used with this system as it was found to give a small increase in captured power compared with an 8s horizon. Figure 22 shows an image of the simplified geometry used for simulation in the WEC-Sim package. We refer the reader back to table I for the important dimensions.

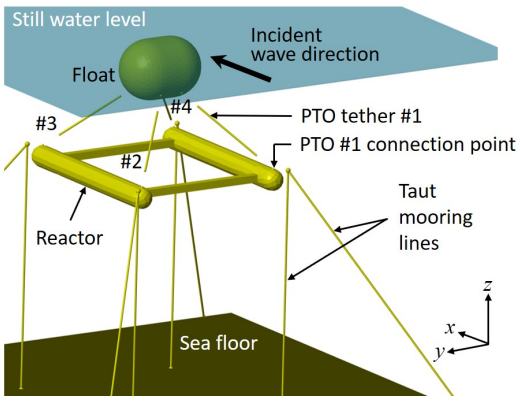

Fig. 22. Simplified geometry and mooring in WEC-Sim

The float and reactor are connected with four taut PTO tether lines, each modelled as a translational PTO actuation force incorporating a spring stiffness and damping force, a universal joint and gimbal. All motions and forces are available for use by the control strategy within this model and the control force applied to each PTO is incorporated by adding to the external preload force on each PTO. The damping force is used only for the benchmark passive optimally tuned system and is set to zero for active control. Irregular waves are applied in the x-direction.

Figure 23 shows the surge (x), heave (z) and pitch (rotation about y) displacement responses of the float in the least energetic sea state ($H_s = 1$m, $T_e = 6$s). We observe that the controlled motions are significantly exaggerated compared to the optimal passive system as we would expect.

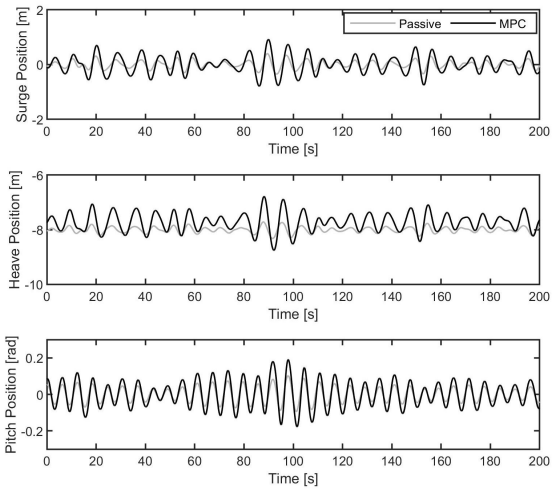

Fig. 23. Surge, heave and pitch displacement responses of the float in Pierson-Moskowitz sea state ($H_s = 1$m, $T_e = 6$s). Results shown for passive system and MPC with 10s horizon

Figure 24 shows the line tensions are also increased compared to the passively controlled system, which leads to increased power capture.

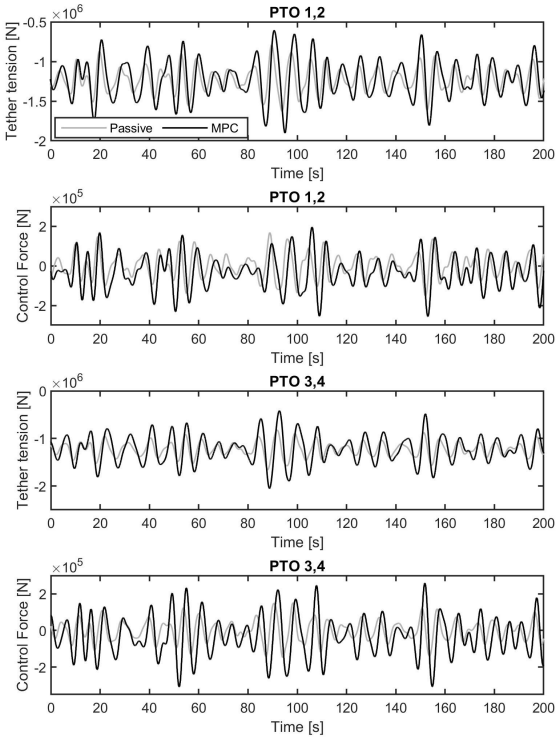

Fig. 24. PTO forces and tether tensions in Pierson-Moskowitz sea state ($H_s = 1$m, $T_e = 6$s) for passive system and MPC with 10s horizon

Figures 25 and 26 show the motions and forces for the sea state $H_s = 3$m, $T_e = 10$s, respectively.

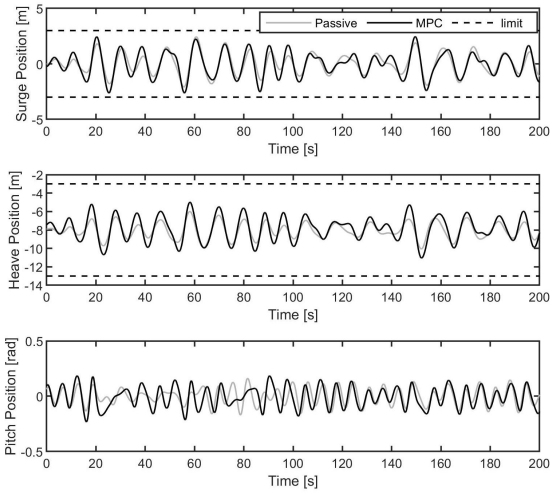

Fig. 25. Surge, heave and pitch displacement responses of the float in Pierson-Moskowitz sea state ($H_s = 3$m, $T_e = 10$s). Results shown for passive system and MPC with 10s horizon

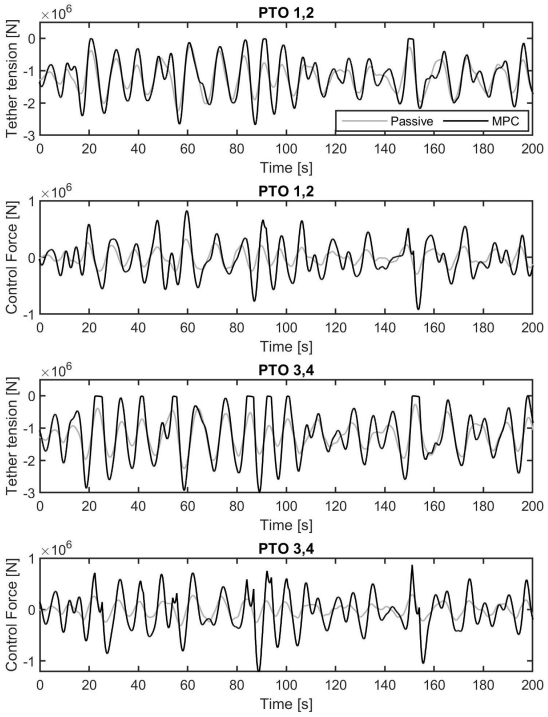

Fig. 26. PTO forces and tether tensions in Pierson-Moskowitz sea state ($H_s = 3$m, $T_e = 10$s) for passive system and MPC with 10s horizon

Constraints on surge and heave displacements are not in danger of being violated and again the motions and PTO line tensions are higher than the passive system, resulting in increased power capture. It can now be seen that the slack line constraint is active from Figure 26, slightly reducing captured power.

Figures 27 and 28 show the displacements and forces for the $H_s = 6$m, $T_e = 16$s sea state. It can now clearly be seen that the MPC law is working to maintain constraints, with large control forces seen at instants to avoid violating position constraints. Displacements are reduced compared to the

passive case, resulting in reduced captured power. However, in terms of power capture this is not a fair comparison as the passive system is not subject to constraints. In reality it is more desirable to reduce the power captured rather than violate the constraints in order to protect the integrity of the WEC. In high energy seas which are above the rated power of the WEC it is desirable to detune the controller, which is effectively what is being done here in an optimal sense. Therefore we argue that the reduced power is not a disadvantage compared to the passive system, rather the ability to incorporate constraints is a significant advantage.

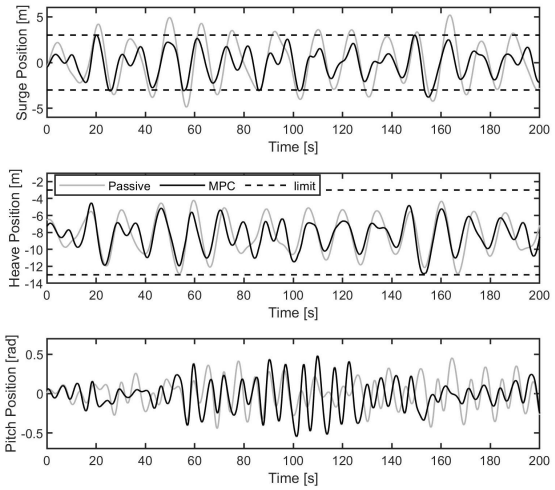

Fig. 27. Surge, heave and pitch displacement responses of the float in Pierson-Moskowitz sea state ($H_s = 6$m, $T_e = 16$s). Results shown for passive system and MPC with 10s horizon

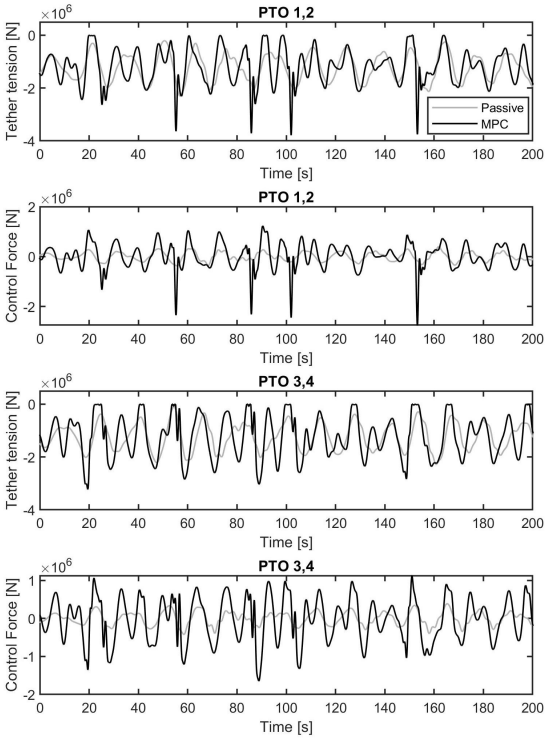

Fig. 28. PTO forces and tether tensions in Pierson-Moskowitz sea state ($H_s = 6$m, $T_e = 16$s) for passive system and MPC with 10s horizon

Figure 29 and table III show the instantaneous and mean absorbed mechanical power for each sea state with the passive and constrained MPC solutions in the three tested sea states.

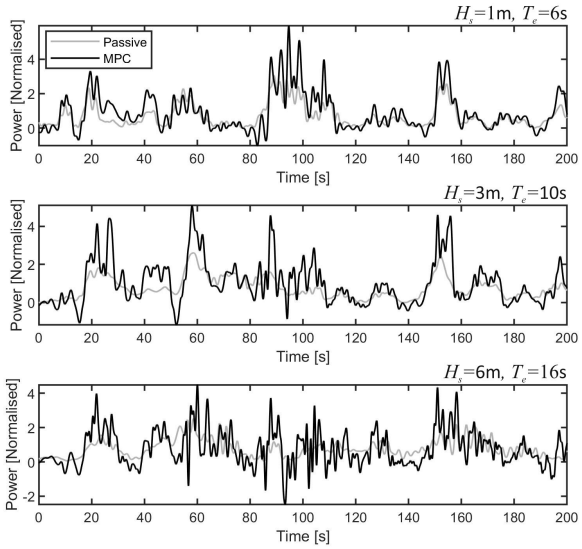

Fig. 29. Instantaneous absorbed power in irregular sea states for WEC-Sim model under passive and constrained MPC control with 10s horizon

TABLE III
MEAN POWER INCREASES COMPARED TO TUNED PASSIVE SYSTEM

Sea State		Mean power ratio (MPC/passive)	
T_e[s]	H_s[m]	Constrained NL state-space	WEC-Sim multibody
6	1	2.62	1.26
10	3	1.66	1.30
16	6	1.15	0.96

Large increases in power are seen for the two lower energy sea states, though not as impressive as seen for the more idealised cases. The highest mean power increase here is +30% in the 10s sea state. The highest energy sea state results in a reduction of absorbed power compared to the passive system of -4%, though as previously stated this power comparison is not meaningful as the passive system was unconstrained. For comparative purposes, the results from simulations using a nonlinear state-space model under constrained MPC are also included in table III. We see a reduction in power capture using the multibody simulation compared with the nonlinear state-space model, which is most pronounced for the least energetic sea state. The reduction is attributed to additional model mismatch as a result of the kinematic transformations required to translate between PTO tether and Cartesian spaces, quadratic viscous damping, and also to the additional slack PTO tether constraint. The large discrepancy seen in the smallest sea state is attributed to amplification of the effects of model mismatch in this particular case. In this lowest energy sea state, the constraints are not active, resulting in large differences in the effectiveness of the controller and subsequent higher velocities and control forces achieved using the simplified state-space model compared to the multibody simulation.

It is also of interest to examine the power flow in PTO pairs. For head-on waves, PTOS 1 and 2, and PTOS 3 and 4, behave in pairs. The power flow in these pairs is shown for the three sea states in Figure 30. The pairs operate out of phase as expected, and the periods where pairs behave as

actuators inputting power to the WEC system can clearly be seen. This raises interesting possibilities for power-sharing power electronic conversion architectures, as explored in [18].

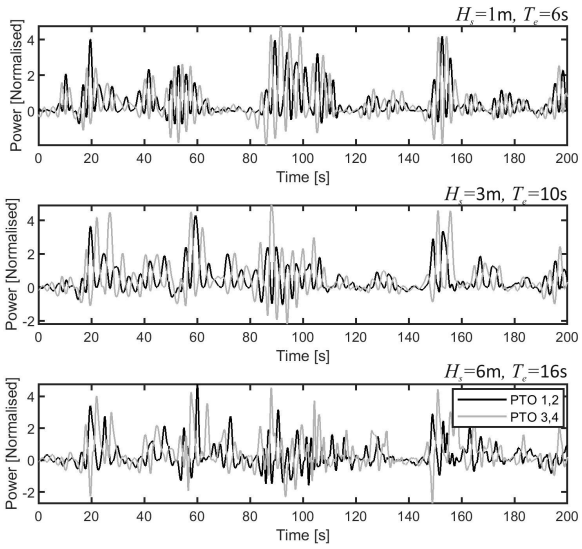

Fig. 30. Instantaneous absorbed power for PTO pairs in irregular sea states for WEC-Sim model under constrained MPC control with 10s horizon

XI. Conclusions

An MPC law has been applied to the multi-DOF WaveSub WEC in idealised and more realistic scenarios with the purpose of investigating the effects of modelling and excitation force prediction errors on system performance. The results show that prediction errors have a significant effect on power absorption, so the choice of prediction horizon is critical to overall system performance. This study considers only a small range of sea states and real sea states may occur which are less predictable, resulting in further degradation of performance. Model mismatch is a significant issue and results in a very large variation in power absorption compared to the ideal case. In part this is due to changes in the controlled system stiffness matrix as the float moves away from its nominal position, and in part because the kinematic Jacobian matrix used to distribute the control forces to the PTO tethers also changes. This could potentially be alleviated by employing a nonlinear MPC law such as in [6], however the already considerable computational burden would further increase along with the risk of infeasibility in the optimisation.

This study, though a step beyond using an idealised state-space model as the target system, is still limited by having at its heart the linearised BEM hydrodynamic coefficients comprising part of the system dynamics. In reality these coefficients will be nonlinear for large motions and complex geometries. Other studies e.g. [8] have shown the sensitivity of system performance to these inaccuracies. The performance results achieved here suggest that significant improvements can still be achieved with an MPC law in spite of these errors. Significant power gains over the optimised passive system were achieved in the more commonly occurring lower energy sea states and the ability to use constraints to limit motion in high energy seas and the tunability of the control law are valuable attributes for practical deployment. However, it is arguably better in reality to use a control strategy that is inherently more robust to uncertainty e.g. the relatively recently proposed pseudo-spectral optimal strategy, see [19] or an AVT strategy as noted in [8]. Indeed, the AVT strategy has been tested by the authors under the same conditions and with the same WEC-Sim model of Wavesub used here and was found to outperform the MPC strategy used here (see [17]).

References

[1] O. Abdelkhalik, S. Zou, G. Bacelli, D. G. Wilson, and R. Coe. Control of three degrees-of-freedom wave energy converters using pseudo-spectral methods. *ASME. J. Dyn. Sys., Meas., Control*, 140(7), 2018.

[2] J.T. Scruggs, S.M. Lattanzio, A.A. Taflanidis, and I.L. Cassidy. Optimal causal control of a wave energy converter in a random sea. *Applied Ocean Research*, 42:1 – 15, 2013.

[3] N. Sergiienko, B. Cazzolato, P. Hardy, B. Ding, and M. Arjomandi. Internal-model-based velocity tracking control of a submerged three-tether wave energy converter. In *Proceedings of the Twelfth European Wave and Tidal Energy Conference*, Cork, Ireland, 2017.

[4] J. Hals, J. Falnes, and T. Moan. Constrained optimal control of a heaving buoy wave-energy converter. *Journal of Offshore Mechanics and Arctic Engineering*, 133(1):011401–011401, 2010.

[5] J.A.M. Cretel, G. Lightbody, G.P. Thomas, and A.W. Lewis. Maximisation of energy capture by a wave-energy point absorber using model predictive control. In *Proceedings of the 18th IFAC World Congress*, Milan, Italy, 2011.

[6] M. Richter, M. E. Magana, O. Sawodny, and T. K. A. Brekken. Nonlinear model predictive control of a point absorber wave energy converter. *IEEE Transactions on Sustainable Energy*, 4(1):118–126, 2013.

[7] A. O'Sullivan. Power maximisation of a wave energy converter using predictive control: Robustness to system mismatch. In A. Lewis, editor, *Proceedings of the Twelfth European Wave and Tidal Energy Conference*, Cork, Ireland, Aug 27–Sep 1 2017. EWTEC.

[8] J. V. Ringwood, A. Mérigaud, N. Faedo, and F. Fusco. An analytical and numerical sensitivity and robustness analysis of wave energy control systems. *IEEE Transactions on Control Systems Technology*, pages 1–12, 2019.

[9] Y. Yu, M. Lawson, K. Ruehl, and C. Michelen. Development and demonstration of the wec-sim wave energy converter simulation tool. In *Proceedings of the 2nd Marine Energy Technology Symposium, Seattle, WA*, 2014.

[10] A. Babarit and G. Delhommeau. Theoretical and numerical aspects of the open source BEM solver NEMOH. In *Proceedings of the 11th European Wave and Tidal Energy Conference*, Nantes, France, 2015.

[11] E. Faraggiana, C. Whitlam, John Chapman, A.J. Hillis, J. Roesner, M. Hann, D. Greaves, Y.-H. Yu, K. Ruehl, I. Masters, G. Foster, and G. Stockman. Computational modelling and experimental tank testing of the multi float wavesub under regular wave forcing. *Renewable Energy*, 2020.

[12] Mohsen N. Soltani, Mahdi T. Sichani, and Mahmood Mirzaei. Model predictive control of buoy type wave energy converter. *IFAC Proceedings Volumes*, 47(3):11159 – 11164, 2014. 19th IFAC World Congress.

[13] Guang Li and Mike R. Belmont. Model predictive control of a sea wave energy converter: a convex approach. *IFAC Proceedings Volumes*, 47(3):11987 – 11992, 2014. 19th IFAC World Congress.

[14] H-N. Nguyen and P. Tona. Wave excitation force estimation for wave energy converters of the point-absorber type. *IEEE Transactions on Control Systems Technology*, 26(6):2173–2181, Nov 2018.

[15] Francesco Fusco and John V. Ringwood. Short-term wave forecasting for real-time control of wave energy converters. *IEEE Transactions on Sustainable Energy*, 1:99–106, 2010.

[16] A.S. Zurkinden, F. Ferri, S. Beatty, J.P. Kofoed, and M.M. Kramer. Non-linear numerical modeling and experimental testing of a point absorber wave energy converter. *Ocean Engineering*, 78:11 – 21, 2014.

[17] A.J. Hillis, C. Whitlam, A. Brask, J. Chapman, and A.R. Plummer. Power capture gains for the wavesub submerged wec using active control. In D. Vicinanza, editor, *Proceedings of the Thirteenth European Wave and Tidal Energy Conference*, Naples, Italy, Sep 1–Sep 6 2019. EWTEC.

[18] A.J. Hillis, A.R. Plummer, X. Zeng, and J. Chapman. Simulation of a power electronic conversion system with short-term energy storage for actively controlled wave energy converters. In *Proceedings of the 6th Offshore Energy and Storage Summit*, Brest, France, 2019.

[19] Giorgio Bacelli and John Ringwood. Numerical optimal control of wave energy converters. *IEEE Transactions on Sustainable Energy*, 6, 04 2015.